Physica A 615 (2023) 128584

Contents lists available at ScienceDirect

Physica A

journal homepage: www.elsevier.com/locate/physa

Physical–statistical learning in resilience assessment for power generation systems

Yiming Che [a], Ziang (John) Zhang [b], Changqing Cheng [a,*]

[a] Department of Systems Science and Industrial Engineering, United States of America
[b] Department of Electrical and Computer Engineering, State University of New York at Binghamton, Binghamton NY 13902, United States of America

ARTICLE INFO

Article history:
Available online 19 February 2023

Keywords:
Basin stability
Sensitivity analysis
Surrogate
Active learning

ABSTRACT

Upswing in extreme weather conditions and natural disasters in conjunction with the relentless penetration of the intermittent renewable energy have brought resilience of the power generation systems into sharp relief. In this study, we adopt a high-order physical model to characterize the full-detail sub-transient behaviors in synchronous generator dynamics, and consequently utilize basin stability (BS) to quantify system resilience against potentially large perturbations. This high-fidelity model has not been extensive probed in estimate of BS, largely owing to the tremendous computational overhead involved. We conduct sensitivity analysis to pick out the most critical system states, whose perturbation exerts huge impact and hence are sensitive on BS or system resilience. Following this, we develop a diversity-enhanced active learning framework to sequentially identify the informative perturbed states, which will be further evaluated by the high-fidelity sub-transient model. This approach only incurs a paltry of simulation effort compared to the crude Monte Carlo simulation but with comparable accuracy on BS estimation.

1. Introduction

As climate change looms large, an alarming uptick in catastrophic weather woes has unfolded globally over the past decades. Indeed, the conflation of such extreme events along with the aging and neglected equipment and antiquated transmission lines engenders the power system susceptible to large perturbations, including abrupt spike in renewable output/ consumer load. The buckling component tends to cascade the perturbation throughout the massive power systems. The latest high-profile deficiencies and failures lay bare the vulnerability of aging U.S. infrastructure. For instance, power grids across the West and South were under exceptional strain in the midst of extreme weather conditions in the first half of 2021, and those large-scale blackouts exacted devastating economical tolls [1–3]. Therefore, resilience concept has been brought to the sharp relief toward the efficacious operation of power systems. It highlights the system's capability to adapt itself to retain basic functionalities amid glitches, failures and environmental disturbances, and is a profound property of many complex systems [4–6]. As a sweeping infrastructure bill has come to pass to revamp the U.S. economy, it is imperative to integrate resilience into such pivotal facility systems to withstand potentially large perturbations or power system faults. Nonetheless, thanks to the highly nonlinear and potentially chaotic dynamics inherent in power

* Corresponding author.
E-mail address: ccheng@binghamton.edu (C. Cheng).

https://doi.org/10.1016/j.physa.2023.128584
0378-4371/

systems (e.g., fluctuation in power supply and demand on the grid, variation of rotator angle in the generator), it remains a confounding quest to attain such resilience.

In nonlinear dynamics theory, stability has been extensively probed in assessment of the resilience for dynamical systems or processes. The dynamical stability indicates that the system returns to the equilibrium states after a transitory period ensuing the onset of perturbations. Conversely, the system states drift away in the midst of loss of stability. Of note, linear stability analysis leverages the largest Lyapunov exponent to assess system resilience when the perturbed states are bounded in vicinity of the equilibrium conditions [7]. That said, it is only amenable to parse vulnerability of dynamical systems against small perturbations. Nonetheless, many realistic dynamical systems including the synchronized dynamics in power generation systems are prone to large perturbations. Worse yet, governing equations for those dynamical systems may be highly nonlinear and/or of higher orders. Accordingly, it is typically formidable to linearize system equations around the equilibrium and formulate the Lyapunov exponent to study the local stability emanating from perturbations. Hence, the method of Lyapunov functions is merely a theoretical advancement and proves difficult to deploy in practice [1]. Hitherto, there has been a persistent drive toward quantifying the stability and resilience of complex dynamical systems against large perturbations.

On the other front, transient stability is a key measure for resilience in power systems [8–11]. It underscores the capability of power generators to maintain the reference grid frequency, also called synchronization, after the transient period in presence of large perturbations, not the least of which include fault on a transmission line, a sudden sea change in renewable throughput and load (or demand), among others. Those perturbations typically lead to considerable excursion of generator rotor angles and frequencies owing to intense variation of the synchronizing torque, as dictated by the intricate relationship between the power and rotor angle of synchronous generation machines [12]. Moreover, the power grids are at the cusp of transformation with the relentless penetration of distributed and intermittent renewable energy sources, and the increasing prevalence of plug-in electric vehicles. This has compounded the operations of the power grid. It bears mentioning that the inverters for renewables are generally not subject to the regulation of grid frequency and susceptible to unstable transients attributed to this inherent low inertia. As a result, the integration of more nonsynchronous inverters into the existing grids is exacting adverse impact on frequency response of the whole power grid and attenuating the grid's capability to damp perturbations, thus posing a quandary for synchronization maintenance. This new normal inevitably leads to unprecedented perturbations that could potentially trigger desynchronization of power generators, and largely suppress the resilience [13].

More recently, basin stability (BS) has garnered tremendous tractions in quantification of transient stability against the arbitrary and large-magnitude perturbations for dynamical systems [7]. It relies on physical or first-principle models, including time-domain simulations [14–16] and energy function approaches [17,18], and consequently incurs huge computational overhead. While such high-fidelity first-principle simulations proliferate in literature, there is a dire need to ameliorate the computational bottleneck. In this present study, we put to test that integration of physical modeling and statistical learning enables efficient and accurate modeling in resilience quantification of power generation systems. In our previous studies [19,20], we applied active leaning to reduce the computational cost. However, they are designed for low dimension systems, and not function well for high dimension systems. Our new approach solves this issue by dimension reduction. We utilize sensitivity analysis (SA) to filter out the critical dimensions and perform the active learning only on these critical dimensions.

2. Background

As the source that generates and exports power to the grid, the electromechanical dynamics of a synchronous generator is foremost for the entire power systems. The rotor motion plays a pivotal role in understanding the dynamical behaviors. Here, we present the physical model that defines the nonlinear and chaotic dynamics of a synchronous power generator.

2.1. Nonlinear dynamics of the synchronous power generator

Different models on power generation systems have been explored in literature, from the simplest second-order swing equation to higher-order models that account for more details for dynamics of generator subcomponent (e.g., the turbine, exciter, and the stabilizer) [5,21,22]. The higher-order model elucidates dynamical behaviors spanning three time periods: sub-transient, transient, and steady state. The sub-transient period spans a short time interval ($\sim$0.03 s) after the short circuit, during which the current is the highest, and accounts for fast dynamics. The transient period comes after elapse of the sub-transient period and lasts till the fault current tapers to a low value, before the post-fault system settles down to a steady state. The control structure for synchronous power generators is implemented in a rotating reference frame, also known as *dq*-reference frame.

Herein, we adopt a 11th-order model to characterize high-resolution generator dynamics, which consists of a 6th-order sub-transient generator model, a 2nd-order exciter model, and a 3rd-order power system stabilizer (PSS) model [23]. We point out that this model provides a more granular view of the generator dynamics, and a new set of time constants (T''_{do} and T''_{qo}) are incorporated to capture fast electromagnetic dynamics. The 6th-order sub-transient model for a synchronous generator machine is defined as follows:

$$T'_{do}\dot{E}'_q = -E'_q - \left(X_d - X'_d\right)\left[I_d - \frac{X'_d - X''_d}{\left(X'_d - X_{ls}\right)^2}\left(\psi_{1d} + \left(X'_d - X_{ls}\right)I_d + E'_q\right)\right] + E_{fd}, \tag{1}$$

Table 1
Notations for the parameters of the 11th-order generator dynamics model.

T'_{do} and T'_{qo}	Transient time constant of d- and q-axis
T''_{do} and T''_{qo}	Sub-transient time constant of d- and q-axis.
X_d and X_q	Synchronous reactance in d- and q-axis
X'_d and X'_q	Transient reactance in d- and q-axis
X''_d and X''_q	Sub-transient reactance in d- and q-axis
H	Inertia constant
D	Damping coefficient
K_A	Voltage regulator gain
V_0	Reference voltage
X_{ls}	Leakage reactance
T_A	Voltage regulator time constant
T_R	Voltage regulator time constant
ω_s	Reference rotor frequency
T_w	PSS Washout time constant
T_{d1}	PSS lag-time Constant 1
T_{d2}	PSS lag-time Constant 2
T_{n1}	PSS lead time Constant 1
T_{n2}	PSS lead time Constant 2
G	PSS gain

$$T''_{do}\dot{\psi}_{1d} = -\psi_{1d} + E'_q - \left(X'_d - X_{ls}\right) I_d, \tag{2}$$

$$T'_{qo}\dot{E}'_d = -E'_d + \left(X_q - X'_q\right)\left[I_q - \frac{X'_q - X''_q}{\left(X'_q - X_{ls}\right)^2}\left(\psi_{2q} + \left(X'_q - X_{ls}\right) I_q + E'_d\right)\right], \tag{3}$$

$$T''_{qo}\dot{\psi}_{2q} = -\psi_{2q} - E'_d - \left(X'_q - X_{ls}\right) I_q, \tag{4}$$

$$\dot{\theta} = \omega - \omega_s, \tag{5}$$

$$\begin{aligned}\frac{2H}{\omega_s}\ddot{\theta} + D\dot{\theta} = P_M &+ \left[\frac{X''_q - X_{ls}}{X'_q - X_{ls}}E'_d - \frac{X'_q - X''_q}{X'_q - X_{ls}}\psi_{2q} + \left(X''_q - X''_d\right) I_q\right] I_d \\ &+ \left[\frac{X''_d - X_{ls}}{X'_d - X_{ls}}E'_q + \frac{X'_d - X''_d}{X'_d - X_{ls}}\psi_{1d}\right] I_q,\end{aligned} \tag{6}$$

Here, P_M denotes the power injection or the mechanical force for this generator, and $\frac{H}{\omega_s}$ is the moment of inertia. By definition, $X_d > X'_d > X''_d > 0$ and $X_q > X'_q > X''_q > 0$ for all synchronous machines. For a synchronous machine to operate in a wide range of operating conditions, it is anticipated to maintain a constant terminal voltage V_{TR}, and thus a constant rotor angle θ and frequency ω. This means that field voltage E_{fd} and mechanical force P_M should be systematically adjusted to accommodate any change in terminal constraints. The physical device that provides the value of P_M is called the prime mover, and that provides value of E_{fd} is called the exciter. A type zero 2nd-order exciter is defined as follows:

$$T_R\dot{V}_{TR} = \sqrt{E_d^2 + E_q^2} - V_{TR}, \tag{7}$$

$$T_A\dot{E}_{fd} = -E_{fd} + K_A\left(V_0 - V_{TR} + S_o\right), \tag{8}$$

A simple 3rd-order power system stabilizer (PSS) is defined as follows [14]:

$$T_w\dot{S}_1 = \omega - S_1, \tag{9}$$

$$T_{d1}\dot{S}_2 = G\left(\omega_s - \frac{T_{n1}}{T_{d1}}\right)(\omega - S_1) - S_2, \tag{10}$$

$$T_{d2}\dot{S}_3 = \left(\omega_s - \frac{T_{n2}}{T_{d2}}\right)\left(\frac{T_{n1}}{T_{d1}}G\left(\omega - S_1\right) + S_2\right) - S_3, \tag{11}$$

$$S_o = \frac{T_{n2}}{T_{d2}}\left(\frac{T_{n1}}{T_{d1}}G\left(\omega - S_1\right) + S_2\right) + S_3, \tag{12}$$

Considering the saturation effects, the transient voltage E'_q has a piecewise function [14]

$$E'_q = \begin{cases} E'_q & if\ E'_q < 0.8 \text{ per unit} \\ 6.980\left(E'_q\right)^2 - 11.236E'_q + 5.322 & Otherwise \end{cases} \tag{13}$$

The nomenclature for the dynamical physical states and the constant parameters of this model is showcased in Table 1 and Table 2, respectively. We follow the notation convention in power systems literature.

After the possibly large perturbation, an excursion is imposed generator states, which are subsequently deemed as the initial condition for a time-domain simulation (TDS) of this high-order model. The perturbed state is stable if the rotor

Table 2
Notations for the physical states of the 11th-order generator dynamics model.

E'_d and E'_q	Transient voltage in d- and q-axis
ψ_d and ψ_q	Flux linkage damper winding in d- and q-axis (uniformly distributed)
E_d and E_q	Terminal voltage in d- and q-axis (uniformly distributed)
I_d and I_q	Current in d- and q-axis
θ	Rotor angle (uniformly distributed)
ω	Rotor frequency (uniformly distributed)
V_{TR}	Generator terminal voltage (uniformly distributed)
E_{fd}	Field voltage (uniformly distributed)
S_1, S_2, S_3	PSS variables (uniformly distributed)
S_o	PSS output

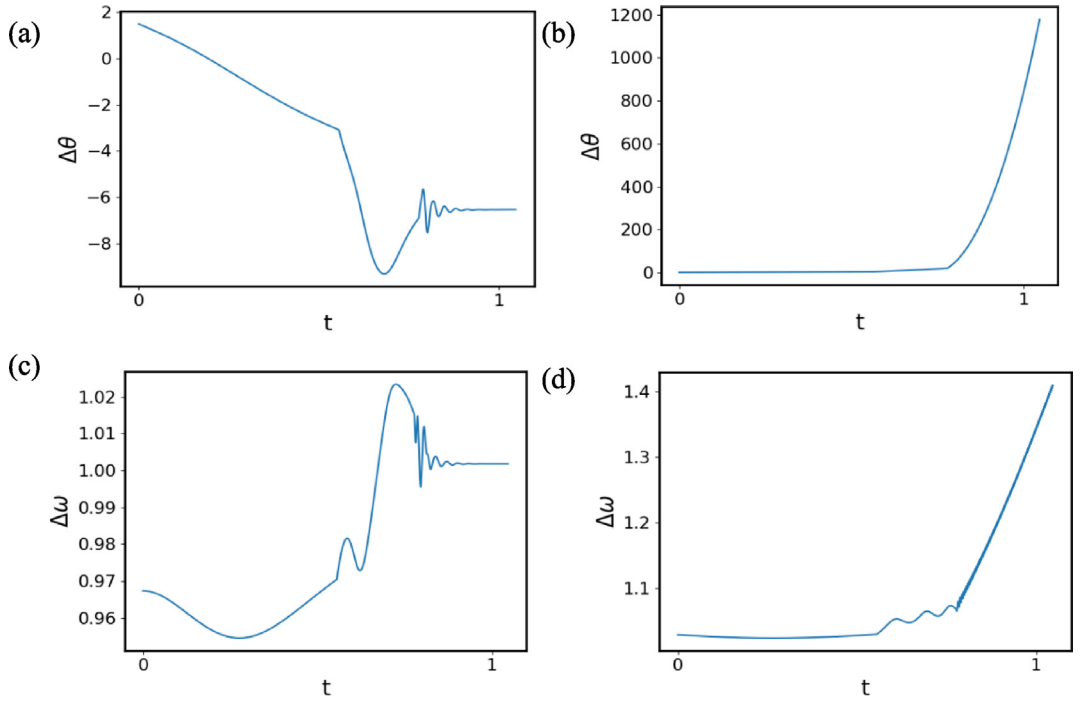

Fig. 1. Evolution of $\Delta\theta$ under (a) stable and (b) unstable dynamics, and evolution of $\Delta\omega$ under (c) stable and (d) unstable dynamics.

angle θ and frequency ω converge to the equilibrium conditions, i.e., the rotor frequency ω coverages to the reference ω_s (60 Hz in the U.S.) and the rotor angle θ maintains a constant discrepancy $\Delta\theta = \theta - \theta_0$ against the reference angle θ_0 in the steady state. The illustration of the stable and unstable dynamics in terms of $\Delta\theta$ and $\Delta\omega = \frac{\omega-\omega_s}{\omega_s}$ following the perturbation from a TDS is depicted in Fig. 1. For simplicity, we only study the stability of the dynamics for one synchronous generator, which corresponds to the single-machine-infinite-bus power grid system. This is a key step in stability analysis of a network of the synchronous generators.

2.2. Basin stability

BS is a benchmark for global stability or resilience of dynamical systems, and it quantifies the likelihood that the dynamical system returns to equilibrium after a large perturbation within a finite time interval. In practice, the large perturbation manifests in a random shift of system state $\boldsymbol{x}$. In a compact form, system dynamics is represented as $\dot{\boldsymbol{x}}(t) = \mathcal{F}(\boldsymbol{x_0}, t)$, with initial condition $\boldsymbol{x_0} \in \mathbb{R}^{\mathrm{d}}$. For power generation systems, system dynamics $\mathcal{F}$ is embodied in the aforementioned 11th-order model (see Eqs. (1)–(13)), and the state $\boldsymbol{x} = \left[\theta, \omega, E_d, E_q, \psi_d, \psi_q, E_{fd}, V_{TR}, S1, S2, S3\right]^T$ is given in Table 2. Here, $[E'_d, E'_q, I_d, I_q, S_o]$ are considered as constant, as they are typically not subject to variations caused by external perturbations. The BS is defined as

$$\mathcal{B} = \int_{\Omega} y(\boldsymbol{x_0})\, \rho(\boldsymbol{x_0})\, d\boldsymbol{x_0}, \tag{14}$$

where $y(\boldsymbol{x_0}) \in 0, 1$ is an indicator function for system convergence to equilibrium from a perturbed $\boldsymbol{x_0}$: $y(\boldsymbol{x_0}) = 1$ indicates $\boldsymbol{x}(t)$ converges to the equilibrium in steady state; $y(\boldsymbol{x_0}) = 0$ otherwise. Ω is the support of probability density

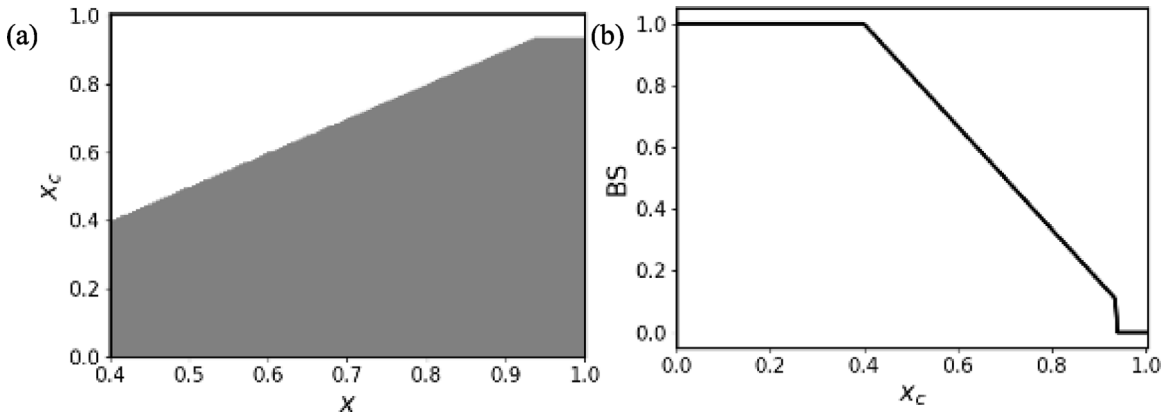

Fig. 2. BS indicates the forewarning as the rainforest degrades: (a) the BoA for the forest state x_1 shrinks and (b) BS diminishes as x_c ticks up.

function $\rho(\boldsymbol{x_0})$ regarding the random perturbation $\boldsymbol{x_0}$, and thus $\int_{\Omega} \rho(\boldsymbol{x_0})\, d\boldsymbol{x_0} = 1$. The set of $\boldsymbol{x_0}$, from which the system returns to equilibrium, is termed as the Basin of Attraction (BoA). Eq. (14) can also be interpreted as $\mathcal{B} = E_\rho[y(\boldsymbol{x_0})] \in [0, 1]$. In other words, BS defines a probability measure that delineates the degree of system resilience considering large perturbations. In practice, BS is approximated by Monte Carlo (MC) sampling. A large number n_{total} of sampling points of $\boldsymbol{x_0}$ are randomly drawn from $\rho(\boldsymbol{x_0})$, according to domain experts or historical data, and then the governing equations are called upon to track the evolution of $\boldsymbol{x}(t)$ on each realization of $\boldsymbol{x_0}$ to assess the convergence. Thereby, BS is estimated as

$$\hat{\mathcal{B}} = \frac{n_e}{n_{total}}, \tag{15}$$

where n_e is the number of sampling points out of n_{total} that converge to equilibrium. The lion's share of existing works on BS involves such tedious MC, and $n_{total} = 1.5 \times 10^6$ was used in our previous work [23]. At issue is the tremendous computational cost to estimate $\hat{\mathcal{B}}$, which is a formidable computational bottleneck. We further elucidate BS with an illustrative example of the Amazonian rainforest [24–26], which bears immense ramification for the earth's climate change. The dynamics of rainforest cover x is encapsulated in a modified Levins model [27]

$$\dot{x} = f(x) = \begin{cases} s(1-x)x - dx & x \geq x_c \\ -dx & x < x_c \end{cases} \tag{16}$$

Here, x_c is a delicate juncture or tipping point, across which x exhibits contrasting dynamics with distinct equilibria, and this bi-stability resides in self-fulfilling feedback dynamics. When $x \geq x_c$, the forest regenerates at a saturating rate s until reaching the fertile forest equilibrium $x_1 = 1 - \frac{d}{s}$ $(s > d > 0)$. A vast forest cover spawns more precipitation and amplifies water concentration in the soil, which further cements vegetation conditions and transpires more water vapors into the atmosphere. Therefore, when the forest cover x is above the decisive tipping point, the Amazon is still able to proliferate amid deforestation and maintains high resilience. Conversely, if $x < x_c$, it degrades with pace d until the rainforest vanishes, pointing to a barren savanna equilibrium $x_2 = 0$. The destructive deforestation scrapes water soaked up in the otherwise rich vegetation, and the landscape withers and tapers off. The forecast becomes more vulnerable to further destruction in this vicious cycle, and eventually saddles into the savanna state.

Remarkably, deleterious human activities juxtaposed with devastating wildfires and dire aridness have exerted outsize perturbations on the Amazonian rainforest over the past decades, which have pushed the rainforest to a precarious status and depleted the resilience against further destructive deforestation, manifesting in the upswing of the tipping point x_c. However, as demonstrated in our prior work, the Lyapunov exponent does not depend on the tipping point x_c, and hence fails to capture loss of stability to the fertile forecast equilibrium x_1, when intensifying aridity ramps up x_c [19]. Consequently, no critical slowing down of recovery from perturbations could be discerned from linear stability. In contrast, BS indicates the forewarning as the rainforest degrades [19]. As shown in Fig. 2 the BoA for the forest state x_1 shrinks (Fig. 2a) and BS diminishes (Fig. 2b) with the elevation of x_c. Whereas BS can be easily computed from MC for this simple case, a fundamental question remains on how to approximate the formidable intricacies and complications of the synchronous generator dynamics.

3. Methodology

To estimate BS of a single generator dynamics described by Eqs. (1)–(13), TDS at 1.5 million realizations of the generator states from a large perturbation was conducted in our prior work [23]. In this exposition, we demonstrate that integration of the high-fidelity physical model with statistical learning offers a unique way to ameliorate the prohibitive computational cost associated with the physical simulation for resilience assessment. This will also pave the way for

optimal resilience design for power grid networks. In essence, BS estimation is a binary classification problem, and the key is to pinpoint the boundary (or boundaries for disjoint BoA) that separates the stable and unstable perturbed system states. Herein, we develop a surrogate classifier, trained from the physical simulation, to asymptotically approximate the boundary. To tackle high dimensionality of the generator states, sensitivity analysis (SA) is first adopted to pick out the most pertinent features among the $d = 11$ generator states, which carry relatively large weight in prescription of the stability boundary according to the XGBoost Classifier. Those states that are not sensitive are treated as constant at their nominal values, i.e., they are not subject to the perturbation. Next, a diversity-enhanced active learning (DAL) framework is leveraged in a sequential sampling strategy, such that only those informative design points that are pivotal to update the decision boundary in each sampling batch are selected and evaluated by the physical model. Hence, we only make occasional recourse to the high-fidelity TDS. This process iterates until the decision boundary converges.

3.1. XGBoost

In machine learning, an ensemble learning enlists a multitude of models to improve prediction accuracy. Boosting is a sequential ensemble technique, which combines a set of base learners to boost learning accuracy in a stage-wise fashion. In gradient boosting machine (GBM), predictive models (e.g., decision trees) are sequentially brought into play to offset residual from the preceding ensemble, and the gradient descent is called upon to fit the new base learner. With training data $\{(\boldsymbol{x}_i, y_i)\}_{i=1}^n$, $\boldsymbol{x}_i \in \mathbb{R}^d$, $y_i \in \mathbb{R}$, for a GBM with K decision trees, the prediction at $\boldsymbol{x}_i$ is derived in an additive way:

$$\hat{y}_i = F_K(\boldsymbol{x}_i) = \sum_{k=1}^{K} f_k(\boldsymbol{x}_i), \tag{17}$$

where f_k is the base learner (decision tree) at iteration k, which has a tree structure q_k and leaf weights $\boldsymbol{w_k} \in \mathbb{R}^{T_k}$. T_k is the number of leaves in the kth tree. The structure q_k maps an instance $\boldsymbol{x}$ to a specific leaf index i, i.e., $q_k : \mathbb{R}^d \to i, i = 1, 2, \ldots, T_k$, and the response of kth tree for $\boldsymbol{x}$ is given as $f_k(\boldsymbol{x}) = \boldsymbol{w_k}[q_k(\boldsymbol{x})]$. That said, $f_k(\boldsymbol{x})$ is a leaf weight with index $q_k(\boldsymbol{x})$. At each iteration k ($k \le K$), the new ensemble is updated as $F_k(x) = F_{k-1}(x) + f_k(x)$, and the new base learner or decision tree $f_k(x)$ is fitted to minimize a loss function $f_k(x) = \arg\min_f L_k = \arg\min_f \sum_{i=1}^n l(y_i, F_{k-1}(x_i) + f_k(x_i))$ via the gradient descent approach. For regression problems, the square error loss function is often used, i.e., $L_K = \sum_{i=1}^n \frac{1}{2}(y_i - F_{k-1} - f_k)^2$. Likewise, XGBoost builds the predictive model additively, albeit with a regularization term $\Omega(f_k) = \gamma T_k + \frac{1}{2}\lambda \|\boldsymbol{w_k}\|^2$ to avoid overfitting. Here, γ is the learning rate, which regulates the complexity of tree q_k. λ is a regularization parameter that penalizes extreme leaf weights $\boldsymbol{w_k}$. Thus, the objective function at iteration k is given as $L_k = \sum_{i=1}^n [l(y_i, F_{k-1}(\boldsymbol{x}_i) + f_k(\boldsymbol{x}_i))] + \Omega(f_k)$. In classification settings for BS estimation, the logistic loss is used instead:

$$l(y_i, \hat{y}_i) = y_i \ln\left(1 + e^{-\hat{y}_i}\right) + (1 - y_i)\ln(1 + e^{\hat{y}_i}) \tag{18}$$

where $\hat{y}_i = \frac{e^{F_k(\boldsymbol{x}_i)}}{1+e^{F_k(\boldsymbol{x}_i)}}$ at iteration k. Yet, this logistic loss function complicates the gradient descent optimization. To this end, the second-order Taylor expansion is adopted on the objective function in XGBoost:

$$L_k = \sum_{i=1}^{n}\left[l(y_i, F_{k-1}) + g_i f_k(\boldsymbol{x_i}) + \frac{1}{2}h_i f_k^2(\boldsymbol{x_i})\right] + \Omega(f_k), \tag{19}$$

where $g_i = \frac{\partial l(y_i, F_{k-1})}{\partial F_{k-1}}$ and $h_i = \frac{\partial^2 l(y_i, F_{k-1})}{\partial (F_{k-1})^2}$. As $l(y_i, F_{k-1})$ is fixed in iteration k, the objective function is simplified as $L_k = \sum_{i=1}^n \left[g_i f_k(\boldsymbol{x}_i) + \frac{1}{2}h_i f_k^2(\boldsymbol{x}_i)\right] + \Omega(f_k)$. We further modify the objective function with the fact that $f_k(\boldsymbol{x}) = \boldsymbol{w_k}[q_k(\boldsymbol{x})]$:

$$L_k = \sum_{j=1}^{T_k}\left[\left(\sum_{i\in I_j} g_i\right) w_{k,j} + \frac{1}{2}\left(\sum_{i\in I_j} h_i + \lambda\right) w_{k,j}^2\right] + \gamma T_k, \tag{20}$$

where I_j represents the set of data points in the jth leaf of the kth tree. Then, given the tree structure q_k, the optimal weight $w_{k,j} = -\frac{G_j}{H_j+\lambda}$, with $G_j = \sum_{i\in I_j} g_i$ and $H_j = \sum_{i\in I_j} h_i$, is obtained by setting $\frac{\partial L_k}{\partial w_{k,j}} = 0$. Consequently, the objective becomes

$$L_{k,q_k} = -\frac{1}{2}\sum_{j=1}^{T_k}\left[\frac{G_j^2}{H_j + \lambda}\right] + \gamma T_k. \tag{21}$$

Identification of the optimal structure q_k is a NP-hard problem. We employ a greedy algorithm and start from a single leaf and then iteratively add leaves with the loss reduction function

$$L_{split} = \frac{1}{2}\left[\frac{G_{I_L}^2}{H_{I_L}+\lambda} + \frac{G_{I_R}^2}{H_{I_R}+\lambda} - \frac{G_I^2}{H_I+\lambda}\right] - \gamma. \tag{22}$$

Here, $I = I_L \cup I_R$; I_L and I_R are the set of data points assigned to the left and right leaves of this leaf node after split. Eq. (22) is the information gain after the split, which also measures the quality of split. We grow the tree with maximal information gain and stop growing when $L_{split} \le 0$.

3.2. Sensitivity analysis

In our prior work, TDS of the generator dynamics model was implemented at $n_{total} = 1.5 \times 10^6$ sampling points of the perturbed physical states in a crude MC simulation to estimate the BS, which is also the ground truth in this study [23]. This number guarantees the variance-to-mean ratio (VMR) as small as 1.27×10^{-7}. To narrow down the critical features amongst the original $d = 11$ physical states that reign supreme in BS estimation, we adopt local sensitive analysis (SA), the one-feature-at-a-time (OFAT) approach. First, we randomly select (e.g., via space filling sampling) a small subset $\mathcal{D}_t = \{\boldsymbol{x_i}, y_i\}_{i=1}^{n_t}$ from the n_{total} data points to train the XGBoost classifier C. Here, $\boldsymbol{x_i} \in \mathbb{R}^d$ and the label $y_i \in 0, 1$ is derived from TDS of the aforementioned physical model. We also select a validation set $\mathcal{D}_v = \{\boldsymbol{x_i}, y_i\}_{i=n_t+1}^{n_t+n_v}$ for SA. For the n_v data points in $\mathcal{D}_v$, in each round we anchor one of the $d = 11$ features to its nominal value at equilibrium and compare the predictive responses from C against the true labels. Specifically, for round $j \in [1, d]$, the jth feature is replaced by its nominal value M^j, i.e., $\boldsymbol{x_i} = \left[x_i^1, x_i^2, \ldots, x_i^d\right]^T$ is replaced with $\boldsymbol{x_i^j} = \left[x_i^1, \ldots, M^j, \ldots, x_i^d\right]^T$ for all $\boldsymbol{x_i} \in \mathcal{D}_v$. We denote the shifted validation set as $\boldsymbol{X^j}$. Then, the predicted responses on the original validation set $\boldsymbol{X}$ and $\boldsymbol{X^j}$ from C are used to derive the accuracy for reach round j: $\varepsilon_j = \frac{\sum_{i=1}^{n_v} \mathbb{I}\left(C(\boldsymbol{x_i}), C(\boldsymbol{x_i^j})\right)}{n_v}$, where $\mathbb{I}(a, b) = \begin{cases} 1 & a = b \\ 0 & \text{otherwise} \end{cases}$. Intuitively, lower accuracy implies high relevance of the feature to system stability, which consequently wields larger impact on the prediction. Hence, we aim to select m of the most pertinent features and derive a compact representation of system dynamics in a m-dimensional subspace. Compared to variance-based and other global SA methods, the OFAT is not computationally intensive. Moreover, computational result in OFAT will be further included in sequential optimal design, thus more appealing that other SA approaches, including Sobol index [28].

3.3. Diversity-enhanced active learning

Given an unlabeled pool $\mathcal{X_u} = \{\boldsymbol{x_i}\}_{i=1}^{n_u} \in \mathbb{R}^d$ whose m pertinent features selected via OFAT vary in the design space and the rest is fixed at nominal value, we seek to select a batch of the most informative $\mathcal{X_k} \subset \mathcal{X_u}$, $|\mathcal{X_k}| = n_k < n_u$ and make recourse to the high-fidelity physical TDS to obtain the label $\boldsymbol{Y_k}$. Then $(\mathcal{X_k}, \boldsymbol{Y_k})$ are annexed into the training set $\mathcal{D}_t$ for further update of the classifier and the stability boundary. This process iterates until the simulation budget is depleted or the estimation is sufficiently close to the true boundary.

To select $\mathcal{X_k}$ from the unlabeled pool $\mathcal{X_u}$, we first identify a pack of candidate points that are most likely to lay close to the true stability boundary, which are the points with large predictive uncertainty from XGBoost. In other words, those design points are more likely to be misclassified. We use the entropy to represent this uncertainty as

$$H_i = -p_0(\boldsymbol{x_i}) \log_2 p_0(\boldsymbol{x_i}) - p_1(\boldsymbol{x_i}) \log_2 p_1(\boldsymbol{x}), \tag{23}$$

where $p_0(\boldsymbol{x_i}) := p(y_i = 0|\boldsymbol{x_i}), p_1(\boldsymbol{x_i}) := p(y_i = 1|\boldsymbol{x_i})$ for $\boldsymbol{x_i} \in \mathcal{X_u}$. Here, $p_0(\boldsymbol{x_i})$ is the output of the classifier C, and $p_1(\boldsymbol{x_i}) = 1 - p_0(\boldsymbol{x_i})$. Theoretically, we could select the top n_c points with maximal summation of entropy, or $\mathcal{X_c} = \text{argmax}_{\boldsymbol{x_1}, \ldots, \boldsymbol{x_{n_c}}} \sum_{i=1}^{n_c} H_i, \boldsymbol{x_i} \in \mathcal{X_u}$, as candidate critical points. Yet, this only leads to the issue of near duplicates, in that those sampling points cluster together and almost duplicate each other. Whereas each design point carries critical information to update the classifier and the boundary, they are not collectively informative. Therefore, the redundant information inherent in near duplicates elevate the computational cost in the TDS without contributing significantly to the stability boundary estimation. To solve the issue of redundancy, we adopt a diversity-enhanced sampling scheme based on the K-means clustering sampling. It is noteworthy that we only adopt diversity sampling on the important features selected by SA. It samples from transformed candidates $\mathcal{X_c} \in \mathbb{R}^d$, whose m pertinent features selected via OFAT vary in the design space and the rest is fixed at nominal value. In concreteness, we first perform K-means clustering algorithm on candidate $\mathcal{X_c}$, then a batch of critical points $\mathcal{X_k} \subseteq \mathcal{X_c}$ that are closest to its nearest cluster center are selected: $\boldsymbol{x_k} = \min_{x \in \mathcal{X_c}} d(\boldsymbol{x}, c_k)$ for $k = 1, \ldots, n_k$, where $d(\cdot, \cdot)$ is the Euclidean distance, c_k is the *kth* cluster center. n_k is the number of clusters and also the size of $\mathcal{X_k}$.

The flowchart of the proposed approach is summarized in Fig. 3. We first conduct SA to select the salient state variables or features that bear profound information in determining the generator stability or synchronization after perturbation. This is carried out on an initial set $\mathcal{D}_t$ with $|\mathcal{D}_t| = n_t$ data points to train the XGBoost classifier. Then, prediction is made on the unlabeled pool $\mathcal{X_u}$, $|\mathcal{X_u}| = n_u$, and predictive entropy is obtained for $\mathcal{X_u}$. The most informative batch of n_c candidate points in $\mathcal{X_c} \in \mathcal{X_u}$ are selected according to the maximal entropy principle. Then, the weighted K-means clustering is conducted on the transformed candidates $\mathcal{X_c}$, i.e., only important features left, and n_k critical design points $\mathcal{X_k}$ are selected according to the distance between candidates and clustering centers. Finally, the responses $\boldsymbol{Y_k}$ are obtained by TDS and $(\mathcal{X_k}, \boldsymbol{Y_k})$ are annexed into the training set $\mathcal{D}_t$ for further update of the classifier.

We halt the training if either of two conditions are met: (1) the simulation budget is exhausted; (2) validation accuracy $\eta = \frac{\sum_{i=1}^{n_v} \mathbb{I}(C(\boldsymbol{x_i}), y_i)}{n_v} \geq 0.9$ and error ratio $\Delta = \frac{|n_{fp} - n_{fn}|}{n_{val}} \leq 1 \times 10^{-3}$ are simultaneously achieved on the validation set, where $\mathbb{I}(C(\boldsymbol{x_i}), y_i) = \begin{cases} 1 & C(\boldsymbol{x_i}) = y_i \\ 0 & otherwise \end{cases}$, $C(\boldsymbol{x_i})$ is the predicted response and y_i is the true response. n_{fp}, n_{fn} and n_{val} are the number of false positive cases, false negative cases on validation set and the size of the validation set.

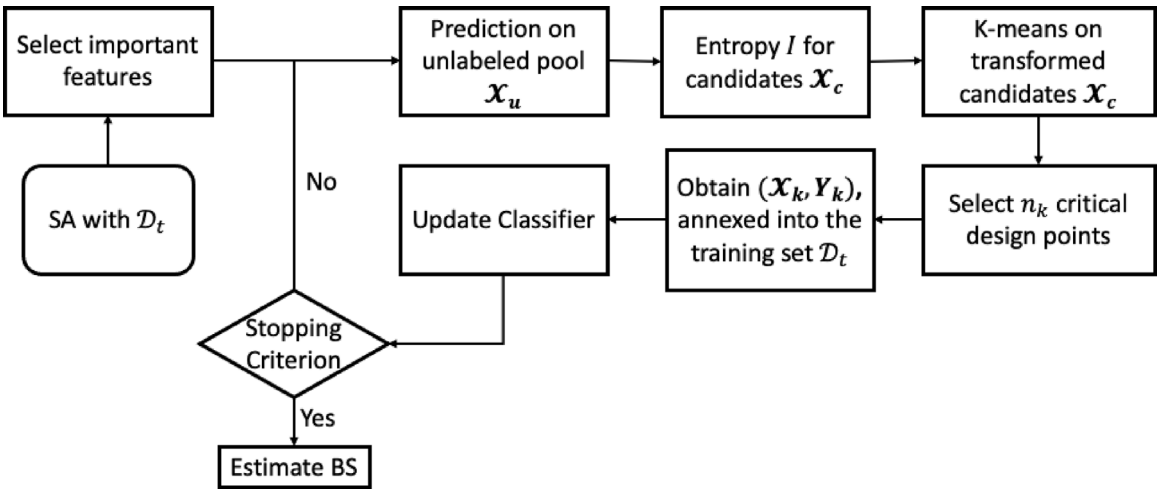

Fig. 3. Roadmap of the proposed method.

Table 3
Lower and upper bounds for the perturbation on physical states.

State variable	$\Delta\omega$	$\Delta\theta$	E'_d	E'_q	ψ_d	ψ_q
$\boldsymbol{L}$	-0.100	$-\pi$	-0.288	-1.001	-0.737	-0.371
$\boldsymbol{U}$	0.100	π	0.546	1.450	1.073	0.751
State Variable	S_1	S_2	S_3	E_{fd}	V_{TR}	
$\boldsymbol{L}$	-6.322×10^{-4}	-1.390	-1.495	-22.813	-0.547	
$\boldsymbol{U}$	7.916×10^{-4}	0.933	0.981	29.796	0.608	

The rationale is that the validation accuracy η alone does not suffice as an optimal stopping criterion, because the error ratio between false positive cases and false negative cases can significantly affect the estimation of BS. We note that BS is estimated as the number of stable sampling points (denoted as positive predictions) over the total number of investigations. In a very special scenario, if we have the same number of false positive (unstable points predicted as stable) and false negative (stable points predicted as unstable) cases on the testing set, then the total number of predicted positive cases will be exactly the same as that of the ground truth and hence, the BS estimation will be exactly the same as the true BS. In addition, if the number of false positive cases is much higher than that of false negative cases on the testing set (1.5 million points), the BS will be overestimated. To this end, we choose $\eta = 0.9$ as the critical validation accuracy and $\Delta = 1 \times 10^{-3}$ as critical error ratio in inference of the whole test set (1.5 million points). This leads to prediction error of $\pm 1 \times 10^{-3}$ on BS estimation. Moreover, the marginal computational cost is too high beyond the threshold of $\eta = 0.9$.

4. Numerical results

Without loss of generalization, we assume the perturbation manifests in the form of a 11-dimensional independent multivariate uniform distribution, and the distribution parameters (the lower bound $\boldsymbol{L}$ and upper bound $\boldsymbol{U}$) for each state variable is shown in Table 3. For the rotor frequency ω and rotor angle θ, we characterize the perturbation on $\Delta\omega$ and $\Delta\theta$: $\Delta\theta \in [-\pi, \pi]$ and $\Delta\omega \in [-0.100, 0.100]$.

In order to determine the optimal size n_t of the initial training set $\mathcal{D}_t$ in SA, we conduct SA with a progressively increasing n_t until the accuracy measure ε_j, or the consistency of the predicted responses on the original validation set $\boldsymbol{X}$ and the shifted set $\boldsymbol{X^j}$, converges. The size of the validation set is fixed as $n_v = 10000$. In Fig. 4, we show the variation of $\varepsilon_j, j = 1, 2, \ldots, 11$ as n_t accrues. With $n_t = 10000$, it is evident that three features notch significantly lower ε_j, suggesting that they are critical toward the stability boundary. Hence, we only include the sensitive features $[\omega, \theta, E'_q]$ to appraise system resilience, and the rest 8 will remain constant at their nominal values. The hyperparameters (the max depth T_k and the number of estimators K) of XGBoost is tuned by 3-fold cross validation on the initial training set $\mathcal{D}_t$: $T_k = 15$ and $K = 100$. We adopt an early stopping rule to prevent overfitting in each iteration: if the metric obtained on the validation set is not further improved after we add another k estimators, we halt the training. Note that the early stopping rule here is to prevent overfitting in each iteration of active learning and is different from the stopping criterion used in the active learning process. In our study, we use the area under ROC curve (AUC) as the performance metric and set $k = 10$.

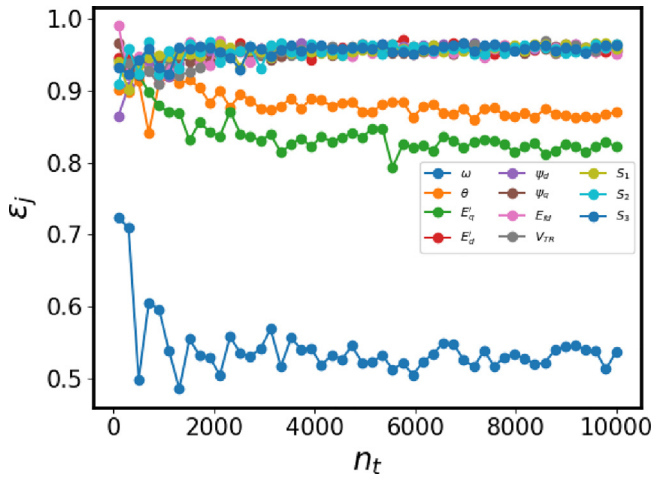

Fig. 4. Variation of the accuracy measure ε_j in SA as n_t increases.

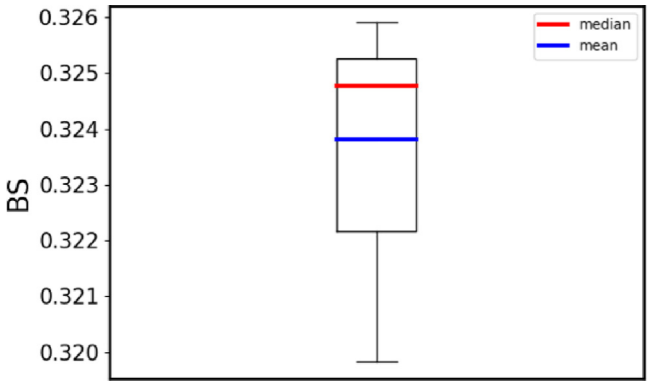

Fig. 5. Boxplot of BS estimation.

The unlabeled pool has a size $n_u = 150000$ in 3-dimensional space. In each iteration of the DAL, we select the most informative $n_k = 300$ design points among the $n_c = 3000$ candidate design points. We set the simulation budget as 200 iterations. We run the experiments 15 times with different initial training set and validation set. The estimated BS are shown in Fig. 5. In these experiments, the mean of BS estimation is 0.3238 with standard deviation 0.0019.

We illustrate the learning process in Fig. 6. In Fig. 6(a), it is evident that we have overfitting at the early learning stage, and the validation accuracy on the testing and validation sets elevates until the iteration halts at iteration 141 according to the stopping criteria. In Fig. 6(b), the error ratio Δ for testing and validation sets showcases oscillation, which affects the BS estimation. The evolution of BS during this learning process is depicted in Fig. 6(c). Whereas it still fluctuates toward the end of the iteration, owing to the oscillation of the error ratio Δ, the computational overhead is considerably high beyond iteration 141, with only marginal improvement on BS estimate.

Furthermore, we visualize the BoA in terms of $\Delta\theta$ and $\Delta\omega$ in Fig. 7, with resolution of 200×200 pixels. Each pixel represents the average BS of design points with the same θ and ω but different valuations for other 9 features, as denoted in the color bar. The approximate BoA at iteration 141 is almost identical to the one obtained under crude MC.

Here, we compare the amount of time used for simple 1.5 million MC simulations and our method. The MC simulation was implemented via parallel computing with machine setting of 12-core CPU (i7-8750H), and the computational time for 1.5 million MC simulations is $\sim$3.5 h. On the same machine setting, the average time used in our methods are $\sim$0.33 h and the training of XGBoost takes $\sim$12 min. In our settings, we implemented K-means from Scikit-learn [29].

5. Conclusions

Uptick in extreme weather conditions and natural disasters and relentless penetration of the renewable energy have posed a quandary for the resilience of the power generating system. In this study, we represent the resilience from a novel

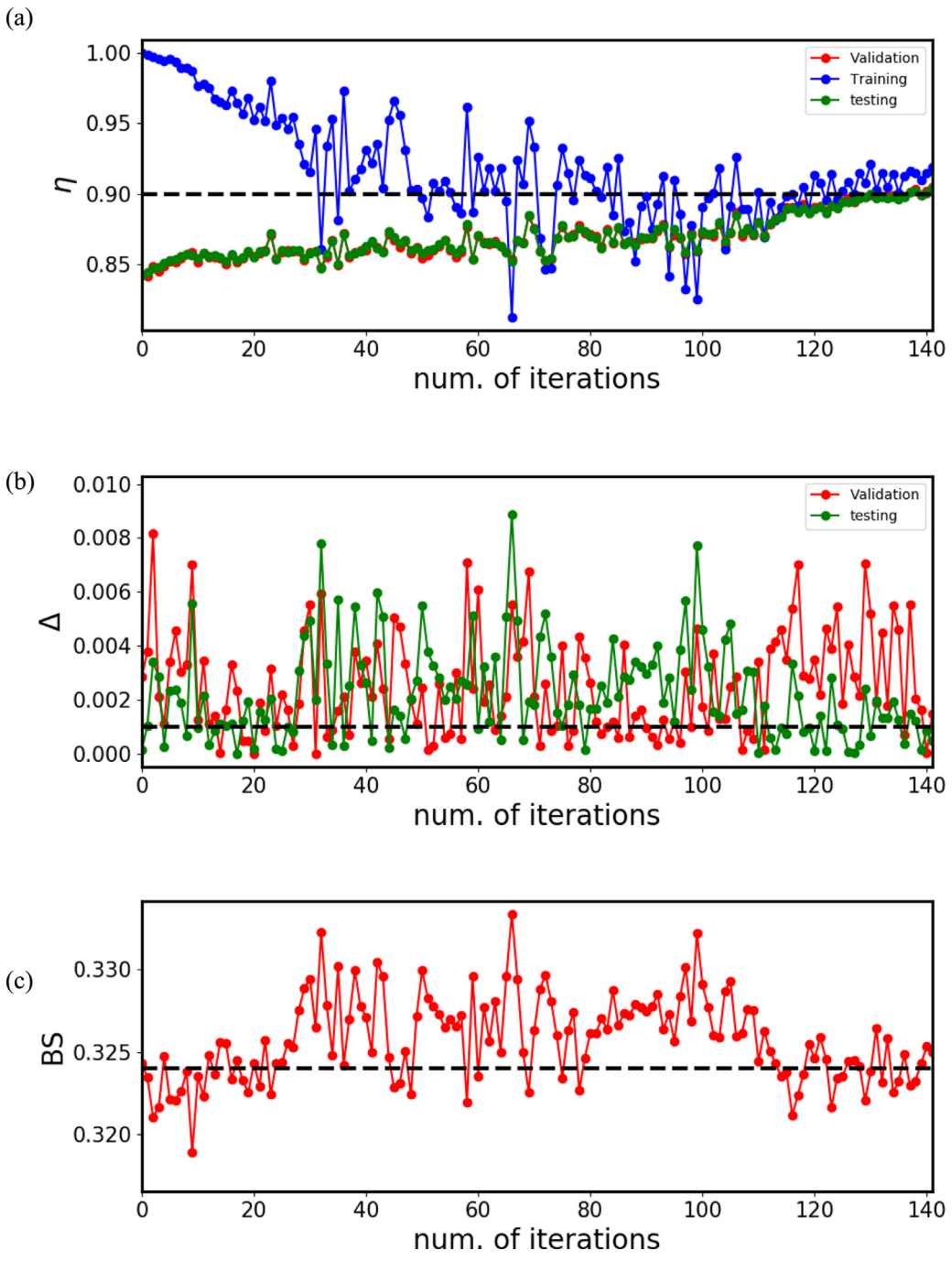

Fig. 6. Training process: (a) training and validation accuracy: The black dashed line is the critical accuracy 0.9; (b) Training and validation error ratio Δ: The black dashed line is the critical ratio 1×10^{-3}; (c) BS estimation: black dashed line is the true BS 0.3240.

perspective of stability of nonlinear dynamic systems, and BS offers a comprehensive measure of system resilience against potentially large perturbations. While models of different fidelities have been explored in literature, from the simplest swing equation to the full-detail sub-transient representation, the high-fidelity models have not been extensive probed in estimate of BS, largely owing to the tremendous computational overhead involved. We adopt sensitivity analysis to pick out the critical states, whose perturbation exerts huge impact and hence are sensitive on BS or system resilience. Following this, we develop a diversity-enhanced active learning framework to sequentially identify the informative perturbed states, which will be further evaluated by the high-fidelity sub-transient model. This approach only incurs a paltry of simulation

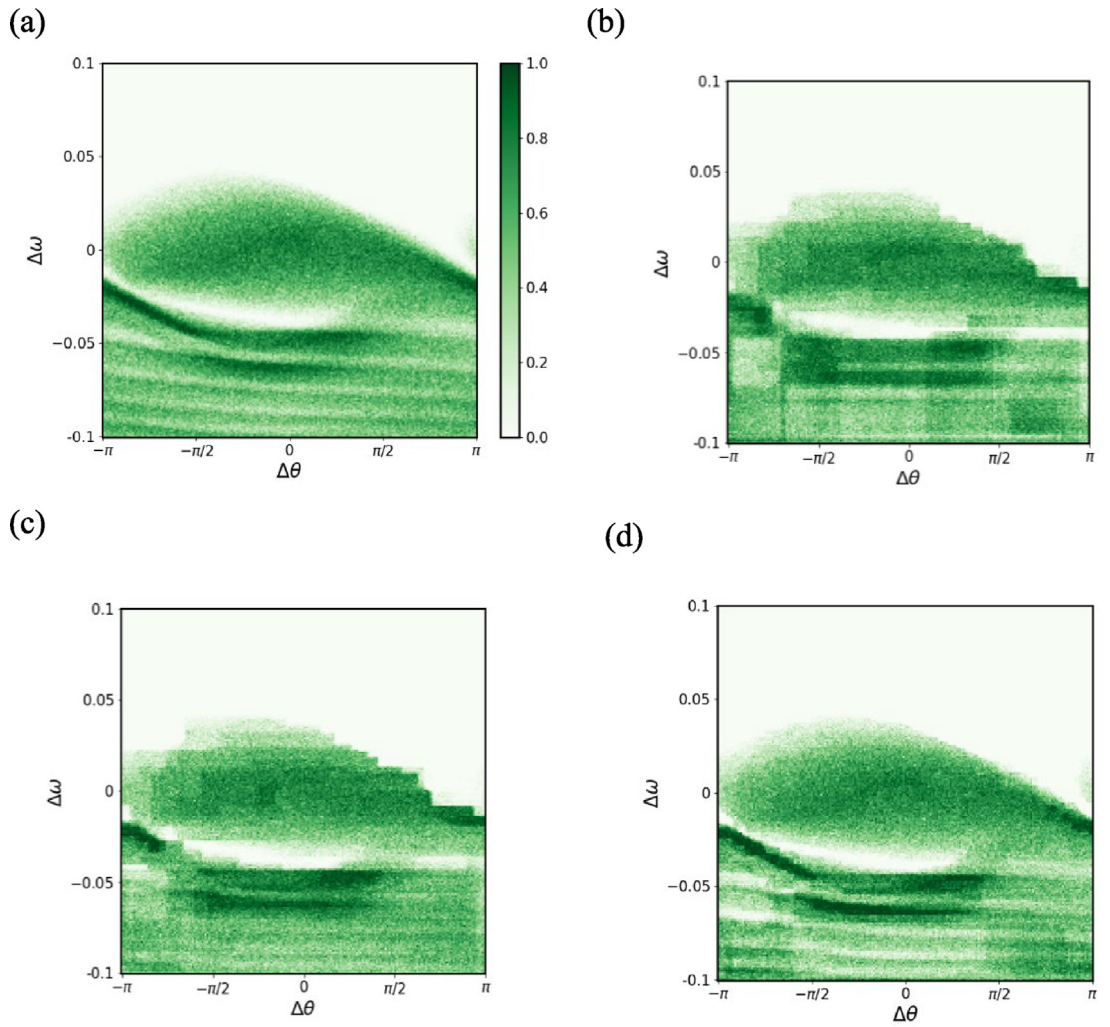

Fig. 7. (a) The 2D BoA from the crude MC method with 1.5 million design points (the underlying truth); (b) (c) (d) the estimated basin plot from the proposed methods at the initial, 50th and the final (141st) iteration.

effort compared to tedious MC simulation but with comparable accuracy on BS estimation. While we only study the BS for a single machine infinite bus system here, this research work also paves the way for the resilience quantification for power grid networks, which can pinpoint the weak generators to reinforcement against potential disruptions.

Declaration of competing interest

The authors declare that they have no known competing financial interests or personal relationships that could have appeared to influence the work reported in this paper.

Data availability

No data was used for the research described in the article.

Acknowledgment

This work is supported by the National Science Foundation, United States (Award Number 2119334) of the United States and the Smart Energy Transdisciplinary Area of Excellence at Binghamton University, United States of America.

References

[1] Timothy Puko, Biden administration to finance $8 Billion in power-grid improvements, Wall Street J. (2021).
[2] John Schwartz, Ivan Penn, Texas power grid, strained last winter, now faces an early heat wave, N.Y. Times (2021).
[3] Katherine Blunt, California blackouts a warning for states ramping up green power, Wall Street J. (2020).
[4] J. Gao, B. Barzel, A.-L. Barabási, Universal resilience patterns in complex networks, Nature 530 (7590) (2016) 307.
[5] S. Auer, K. Kleis, P. Schultz, J. Kurths, F. Hellmann, The impact of model detail on power grid resilience measures, Eur. Phys. J. Spec. Top. 225 (3) (2016) 609–625.
[6] R. Cohen, K. Erez, S. Havlinl, M. Newman, A.-L. Barabási, D.J. Watts, Resilience of the internet to random breakdowns, in: The Structure and Dynamics of Networks, Princeton University Press, 2011, pp. 507–509.
[7] P.J. Menck, J. Heitzig, N. Marwan, J. Kurths, How basin stability complements the linear-stability paradigm, Nat. Phys. 9 (2013) 89.
[8] A. Mitra, D. Chatterjee, Active power control of DFIG-based wind farm for improvement of transient stability of power systems, IEEE Trans. Power Syst. 31 (1) (2015) 82–93.
[9] P.N. Papadopoulos, J.V. Milanović, Probabilistic framework for transient stability assessment of power systems with high penetration of renewable generation, IEEE Trans. Power Syst. 32 (4) (2016) 3078–3088.
[10] M. Ayar, S. Obuz, R.D. Trevizan, A.S. Bretas, H.A. Latchman, A distributed control approach for enhancing smart grid transient stability and resilience, IEEE Trans. Smart Grid 8 (6) (2017) 3035–3044.
[11] A. Farraj, E. Hammad, D. Kundur, A cyber–physical control framework for transient stability in smart grids, IEEE Trans. Smart Grid 9 (2) (2016) 1205–1215.
[12] P. Kundur, et al., Definition and classification of power system stability IEEE/CIGRE joint task force on stability terms and definitions, IEEE Trans. Power Syst. 19 (3) (2004) 1387–1401, http://dx.doi.org/10.1109/TPWRS.2004.825981.
[13] A.E. Motter, S.A. Myers, M. Anghel, T. Nishikawa, Spontaneous synchrony in power-grid networks, Nat. Phys. 9 (2013) 191–197.
[14] J.H. Chow, K.W. Cheung, A toolbox for power system dynamics and control engineering education and research, IEEE Trans. Power Syst. 7 (4) (1992) 1559–1564, http://dx.doi.org/10.1109/59.207380.
[15] C.D. Vournas, E.G. Potamianakis, C. Moors, T. Van Cutsem, An educational simulation tool for power system control and stability, IEEE Trans. Power Syst. 19 (1) (2004) 48–55, http://dx.doi.org/10.1109/TPWRS.2003.821016.
[16] H. Morais, P. Vancraeyveld, A.H.B. Pedersen, M. Lind, H. Johannsson, J. Ostergaard, SOSPO-SP: Secure operation of sustainable power systems simulation platform for real-time system state evaluation and control, IEEE Trans. Ind. Inform. 10 (4) (2014) 2318–2329, http://dx.doi.org/10.1109/TII.2014.2321521.
[17] H.-D. Chiang, J.S. Thorp, The closest unstable equilibrium point method for power system dynamic security assessment, IEEE Trans. Circuits Syst. 36 (9) (1989) 1187–1200, http://dx.doi.org/10.1109/31.34664.
[18] T. Athay, R. Podmore, S. Virmani, A practical method for the direct analysis of transient stability, IEEE Trans. Power Appar. Syst. PAS-98 (2) (1979) 573–584, http://dx.doi.org/10.1109/TPAS.1979.319407.
[19] Y. Che, C. Cheng, Z. Liu, Z.J. Zhang, Fast basin stability estimation for dynamic systems under large perturbations with sequential support vector machine, Physica D 405 (2020) 132381.
[20] Y. Che, C. Cheng, Active learning and relevance vector machine in efficient estimate of basin stability for large-scale dynamic networks, Chaos 31 (5) (2021) 053129.
[21] T.W. Stegink, C. De Persis, A.J. Van Der Schaft, An energy-based analysis of reduced-order models of (networked) synchronous machines, Math. Comput. Model. Dyn. Syst. 25 (1) (2019) 1–39.
[22] T. Weckesser, H. Jóhannsson, J. Østergaard, Impact of model detail of synchronous machines on real-time transient stability assessment, in: 2013 IREP Symposium Bulk Power System Dynamics and Control-IX Optimization, Security and Control of the Emerging Power Grid, 2013, pp. 1–9.
[23] Z. Liu, X. He, Z. Ding, Z. Zhang, A basin stability based metric for ranking the transient stability of generators, IEEE Trans. Ind. Inform. 15 (3) (2018) 1450–1459.
[24] L. Da Silveira Lobo Sternberg, Savanna–forest hysteresis in the tropics, Global Ecol. Biogeogr. 10 (4) (2001) 369–378.
[25] M. Hirota, M. Holmgren, E.H. Van Nes, M. Scheffer, Global resilience of tropical forest and Savanna to critical transitions, Science 334 (6053) (2011) 232–235.
[26] R.M. May, Thresholds and breakpoints in ecosystems with a multiplicity of stable states, Nature 269 (5628) (1977) 471.
[27] P.J. Menck, J. Heitzig, N. Marwan, J. Kurths, How basin stability complements the linear-stability paradigm, Nat. Phys. 9 (2) (2013) 89.
[28] I.M. Sobol, Global sensitivity indices for nonlinear mathematical models and their Monte Carlo estimates, Math. Comput. Simulation 55 (1–3) (2001) 271–280.
[29] F. Pedregosa, et al., Scikit-learn: Machine learning in Python, J. Mach. Learn. Res. 12 (2011) 2825–2830.